Thin-section Ratiometric Ca^{2+} Images Obtained by Optical Sectioning of Fura-2 Loaded Mast Cells

Jonathan R. Monck, Andres F. Oberhauser, Thomas J. Keating, and Julio M. Fernandez

Department of Physiology and Biophysics, Mayo Clinic, Rochester, Minnesota 55905

Abstract. The availability of the ratiometric Ca^{2+} indicator dyes, fura-2, and indo-1, and advances in digital imaging and computer technology have made it possible to detect Ca^{2+} changes in single cells with high temporal and spatial resolution. However, the optical properties of the conventional epifluorescence microscope do not produce a perfect image of the specimen. Instead, the observed image is a spatial low pass filtered version of the object and is contaminated with out of focus information. As a result, the image has reduced contrast and an increased depth of field. This problem is especially important for measurements of localized Ca^{2+} concentrations. One solution to this problem is to use a scanning confocal microscope which only detects in focus information, but this approach has several disadvantages for low light fluorescence measurements in living cells. An alternative approach is to use digital image processing and a deblurring algorithm to remove the out of focus information by using a knowledge of the point spread function of the microscope. All of these algorithms require a stack of two-dimensional images taken at different focal planes, although the "nearest neighbor deblurring" algorithm only requires one image above and below the image plane.

We have used a modification of this scheme to construct a simple inverse filter, which extracts optical sections comparable to those of the nearest neighbors scheme, but without the need for adjacent image sections. We have used this "no neighbors" processing scheme to deblur images of fura-2–loaded mast cells from beige mice and generate high resolution ratiometric Ca^{2+} images of thin sections through the cell. The shallow depth of field of these images is demonstrated by taking pairs of images at different focal planes, 0.5-μm apart. The secretory granules, which exclude the fura-2, appear in focus in all sections and distinct changes in their size and shape can be seen in adjacent sections. In addition, we show, with the aid of model objects, how the combination of inverse filtering and ratiometric imaging corrects for some of the inherent limitations of using an inverse filter and can be used for quantitative measurements of localized Ca^{2+} gradients. With this technique, we can observe Ca^{2+} transients in narrow regions of cytosol between the secretory granules and plasma membrane that can be less than 0.5-μm wide. Moreover, these Ca^{2+} increases can be seen to coincide with the swelling of the secretory granules that follows exocytotic fusion.

THE concentration of cytosolic-free Ca^{2+} has been implicated in the regulation of many biological processes, including muscle contraction, secretion, and regulation of metabolism (Berridge, 1987; Williamson and Monck, 1989). Consequently, it is important to be able to measure the cytosolic Ca^{2+} concentration. Such measurements were revolutionized by the introduction of the fluorescent Ca^{2+} indicator molecule quin2 and, subsequently, the ratiometric dyes, fura-2, and indo-1 (Tsien, 1980; Grynkiewicz et al., 1985; Tsien, 1989). The ratiometric dyes exhibit a shift in the excitation (fura-2) or emission (indo-1) spectra upon binding Ca^{2+} which allows calibration of the cytosolic Ca^{2+} concentration with a simple ratiometric procedure that corrects for differences in light path length and indicator concentration (Grynkiewicz et al., 1985). The combination of fura-2 measurements with recent advances in digital imaging and computer technology has made it possible to detect some interesting temporal and spatial changes in the intracellular Ca^{2+} concentration in single cells (Cohan et al., 1987; Wier et al., 1987; Connor et al., 1987; O'Sullivan et al., 1989; Monck et al., 1990*a*; Rooney et al., 1990).

The detection of localized Ca^{2+} concentrations using a conventional epifluorescence microscope is limited because the finite numerical aperture of the objective results in distortion of the image and reduced image contrast. The light emanating from an ideal point source becomes spread out and takes on a characteristic three-dimensional shape, the point spread function, or PSF (Castleman, 1979; Agard, 1984). As a result the observed image is blurred and is contaminated with out-of-focus light. The problem is most significant in the axial direction so that the apparent depth of field is increased. If part of a cell has a localized high

Ca^{2+} concentration, then light from this region will be contaminated with out-of-focus light from parts of the cell with a lower Ca^{2+} concentration and the apparent gradient will be smaller and more spread out than the real gradient. In practice this has meant that measurement of localized Ca^{2+} concentration has been restricted to cells with distinct structures such as neurons with prominent axons and dendritic processes (Cohan et al., 1987; Lipscombe et al., 1988), flattened cells in which it has been possible to see waves of Ca^{2+} propagating across single cells and between adjacent cells (Cornell-Bell et al., 1990; Rooney et al., 1990), and cells where localized changes occur in relatively large regions of the cell such as the nucleus or areas rich in ER (Williams et al., 1985; Connor et al., 1987; O'Sullivan et al., 1989). However, it has not been possible to measure localized changes in small rounded cells.

One solution to the problem of image distortion by the light path is to use one of the various types of scanning confocal microscopes (Brakenhoff et al., 1989; Wright et al., 1989; Shotton, 1989; Lichtman et al., 1989). In confocal microscopy the object is illuminated with a diffraction-limited spot, usually using a focused laser beam, and the light reaching the detector is spatially restricted by a pinhole aperture placed in an image plane in front of the detector, so that out of focus light is excluded. An image is built up by scanning through the image plane point-by-point either by moving the illuminated point (laser scanning) or the specimen (stage scanning). Thus each point in a confocal image contains light mainly from a corresponding point in the object. The result is an image with greatly improved axial resolution and also an improved lateral resolution (Brakenhoff et al., 1989; Shotton, 1989; Inoue, 1990). The tandem-scanning confocal microscope uses a similar principle except that, instead of using a laser, an illuminating aperture is scanned relative to a stationary optical beam and stationary specimen by rapidly rotating a Nipkow disk containing several thousand pairs of diametrically opposed apertures, one serving as the illumination aperture and its pair as the exit pinhole. A similar approach is used in the spiral scanning confocal microscope, except that the same pinholes in the Nipkow disk are used for both illumination and exit pinholes.

For Ca^{2+} measurements the scanning confocal microscopes have several disadvantages. First, there are technical difficulties in using the dual excitation or emission indicators. Therefore, differences in dye concentration or differences in the path length due, for example, to small organelles that exclude the indicator molecule cannot be corrected for using the ratiometric procedures that make fura-2 and indo-1 the normal indicators of choice (Tsien, 1989). Second, for measurement of the low light intensities typical of Ca^{2+} measurements in small cells the amount of light collected can become limiting because of the requirement to scan the pixels sequentially, and in the case of the laser scanning microscopes, because the mirrors and optical elements necessary for the scanning have a low total transmission (Wells et al., 1990). This can be overcome by increasing the illumination intensity but high illumination intensities can, in some cases, cause problems of fluorophore saturation, increased photobleaching and/or increased photocytotoxicity (Wells et al., 1990; Tsien and Waggoner, 1990). For any of the scanning confocal microscopes the detected signal can be increased by increasing the size of the exit pinhole or by replacing the pinhole with a slit (Lichtman et al., 1989), but at the expense of reduced rejection of out of focus light. This probably explains why reports of confocal Ca^{2+} measurements have mainly used fluo-3 in relatively large cells (Hernandez-Cruz et al., 1990; Wright et al., 1989; Niggli and Lederer, 1990).

An alternative means of achieving an optical section with a shallow depth of field is to collect the images using a conventional microscope and correct for out of focus information and image distortion using digital image processing techniques and a knowledge of the point spread function of the microscope. Several such procedures have been developed for extracting pure optical sections before reconstruction of three-dimensional images from a stack of two-dimensional images (Castleman, 1979; Agard, 1984; Agard et al., 1989; Fay et al., 1989). One relatively simple procedure, the "nearest neighbors deblurring scheme" assumes that light from adjacent sections (i.e., images obtained with a known shift in the focus) accounts for the majority of the out of focus information (Weinstein and Castleman, 1971; Castleman, 1979; Gruenbaum et al., 1984; Agard, 1984). The contribution of light from the neighboring sections is estimated by blurring the adjacent sections by convolution with the out of focus point spread function. These blurred images are then subtracted from the in focus section and finally the image is sharpened by convolution with a Wiener inverse filter. After processing, the signal remaining in each pixel in the image corresponds predominantly to light from a confocal point in the object.

For time-resolved Ca^{2+} measurements, the requirement to take several images at different focal planes is a major disadvantage. Ideally, one would be able to apply a two-dimensional inverse filter to a single image to obtain a thin section through the cell. In this study, we have used a simple modification of the nearest neighbors deblurring scheme to obtain ratiometric fura-2 images from mast cells. We show that when the in focus image is used instead of adjacent image planes for the deblurring, the restored image is almost identical to that obtained using the nearest neighbors scheme. The processed images have greatly reduced blurring and reduced depth of field and allow measurement of the cytosolic Ca^{2+} concentration in small regions of the image plane between the plasma membrane and secretory granule that are less than 0.5 μm across.

Materials and Methods

Mast Cell Preparation

Mast cells were prepared from adult beige (bg^j/bg^j) mice (Jackson Laboratories, Bar Harbor, ME) as described previously (Monck et al., 1990*b*). Briefly, mouse peritoneal mast cells were obtained by a peritoneal lavage, plated onto glass bottom culture chambers, and stored at 37°C under a 5% CO_2 atmosphere until use. The medium for this incubation contained (in millimolar): 136 NaCl, 10 Hepes, 0.8 NaOH, 0.9 $MgCl_2$, 1.8 $CaCl_2$, 45 $NaHCO_2$, 0.8 K_2HPO_4, 2.5 glucose (pH 7.2). For experiments, the incubation medium was replaced by a modified Ringer's solution containing (in millimolar): 150 NaCl, 10 Hepes, 2.8 KOH, 1.5 NaOH, 1 $MgCl_2$, 2 $CaCl_2$, and 25 glucose (310 mmol/kg; pH 7.25).

The Optical Sectioning Microscope System

Our experiments were done on a microscope system built around an inverted IM 35 microscope (Carl Zeiss, Oberkochen, Germany) equipped with a

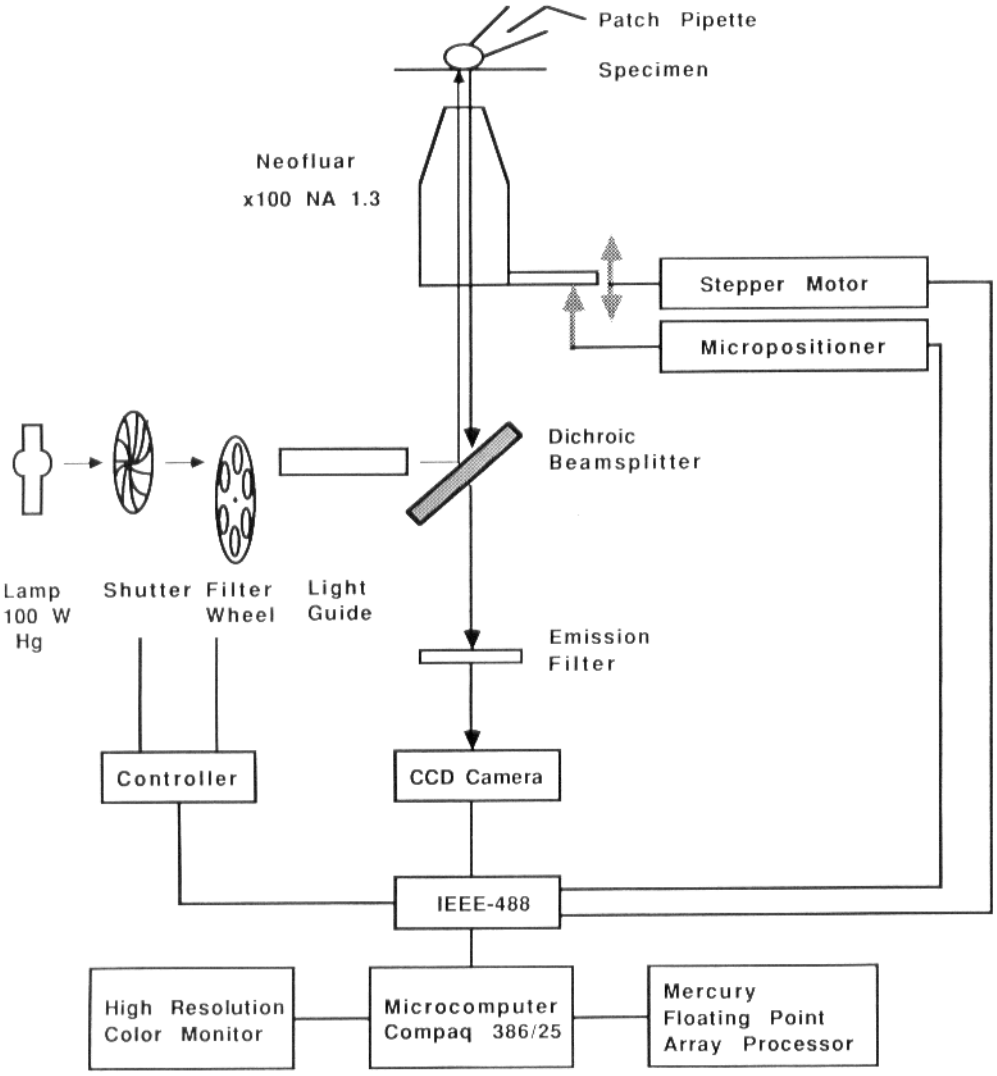

Figure 1. Schematic representation of the apparatus used for fluorescence measurements. Epifluorescence measurements were made using a Zeiss inverted IM35 microscope equipped with either a Zeiss Neofluar (×100, NA 1.3) or Zeiss Planapo (×63, NA 1.4) objective. Light from a 100 W mercury lamp was passed through a shutter and filter wheel assembly and coupled to the microscopic epifluorescence attachment with a 1-mm diam silica optical fiber. Fluorescence images were acquired with a peltier cooled CCD camera. A stepper motor was used to change the focus and a micropositioner gave an accurate measure of the focal position. An IEEE-488 interface was used to control the filter wheel, micropositioner, stepper motor, and CCD camera remotely from the microcomputer. Images from the CCD camera were transferred to the microcomputer and processed on a 20 MFLOPS floating point array processor.

peltier cooled (−40°C) charge coupled device (CCD) camera (Photometrics, Ltd., Tucson, AZ). The CCD chip was a 1,024 × 1,000 pixel TI 215-30 (Texas Instruments, Lubbock, TX) and images were collected with 12-bit resolution. The camera and several other devices were controlled from a microcomputer (Compaq Desk Pro 386/25; Compaq Computer Corporation, Houston, TX) using an IEEE-488 interface (National Instruments, Austin, TX). Fig. 1 shows the microscope system with the epifluorescence pathway in schematic form. A stepper motor (model MC 2000; Daedal, Inc., Harrison City, PA) was attached to the fine focus of the microscope, enabling the focus to be moved under computer control. The exact position of focus was determined using a micropositioner (model MT 25; Heidenhain Corporation, Elk Grove Village, IL.). The micropositioner returns a number at 0.5-μm intervals. However, by slowly stepping the motor until the transition between two values occurred, accuracy better than 0.1 μm could be obtained.

A 100 W mercury lamp housing (Carl Zeiss) was attached to a shutter-filter wheel assembly (Ludl Electronic Products, Ltd., Scarsdale, NY). This device allowed us to change excitation wavelength and control the time of exposure under computer control. An ultraviolet transmitting silica fiber (2 m length; 1-mm diam; General Fibre, Cedar Grove, NJ) was used to couple the lamp assembly to the epifluorescence attachment of the IM-35 microscope. The scrambled light from the light guide was collimated with a quartz convex lens. The original lenses in the Zeiss epifluorescence attachment were removed. Images collected by the CCD camera were transferred to a Mercury floating point array processor (model MC 3200, Mercury Computer Systems, Inc., Lowell, MA) for image manipulation. The computer programs (available on request) for data collection, control of various devices, image processing on the Mercury and display were custom written as modules running with the Image Pro software package (Media Cybernetics, Silver Spring, MD). Images were displayed using a PepperPro high resolution video interface (Number Nine Computer Corporation, Cambridge, MA) and Mitsubishi high resolution color monitor (Mitsubishi Electric Corporation, Tokyo, Japan) or on a Silicon Graphics Personal Iris work station using the ANALYZE software package (Biodynamics Research Unit, Mayo Clinic, Rochester, MN).

Image Processing Schemes for Extraction of Optical Sections

The image processing scheme is a modification of the nearest neighbors scheme used by Agard and colleagues to remove out of focus information from each of a stack of two-dimensional sections before reconstruction of a three-dimensional image. To explain our scheme it is useful to briefly summarize the assumptions and equations underlying the nearest neighbors scheme (for a more complete description see Castleman, 1979; Agard, 1984; Agard et al., 1989). It is assumed that all the light in the observed image is contributed by the in focus image plane and the two adjacent image planes:

$$o_j = i_j * s_o + i_{j+1} * s_1 + i_{j-1} * s_{-1}$$

where o_j is the observed image; i_j the actual in-focus image; i_{j+1} and i_{j-1} the images in the neighboring planes; s_o the in focus point spread function; and s_1 and s_{-1} the out of focus point spread functions (we have used the

1. *Abbreviations used in this paper*: CCD, charge-coupled device; CTF, contrast transfer function; GTPγS, guanosine-5'-o-(3-thiotriphosphate); PSF, point spread function.

same notation as Agard et al., 1989). The * represents a convolution operator (Castleman, 1979). By taking the Fourier transformation of both sides of the equation the convolution operator can be replaced by a simple multiplication:

$$O_j = I_j S_o + I_{j+1} S_1 + I_{j-1} S_{-1}$$

where S_1 and S_o are now the contrast transfer functions, the Fourier transforms of the point spread functions. Then if it is assumed that O_{j+1} and O_{j-1} can be used as approximations for I_{j+1} and I_{j-1}, and ignoring the slight difference between S_1 and S_{-1}, the equation can be rewritten:

$$I_j = [O_j - c(O_{j+1} + O_{j-1})S_1]/S_o$$

where c is an empirical constant. One problem with using the inverse of S_o as a filter is that at high spatial frequencies noise will dominate. A solution to this problem is to replace $1/S_o$ with a Wiener inverse filter (Agard et al., 1989).

For processing our images we have used a modification of the nearest neighbors deblurring scheme, which we will refer to as the no neighbors deblurring scheme. An exception is in Fig. 2 in which we use the nearest neighbors scheme itself for direct comparison. The nearest neighbors approach assumes that, for the purposes of the blurring, the true images in the adjacent planes can be replaced by the observed images, i.e., that $I_{j+1}S_1$ and $I_{j-1}S_1$ can be approximated by $O_{j+1}S_1$ and $O_{j-1}S_1$. We wanted to be able to avoid the need for taking three sections for time course measurements of Ca^{2+} concentration. Therefore, we made the additional assumption that the blurred image (O_jS_1) can be used instead of the blurred neighbors ($O_{j+1}S_1$ and $O_{j-1}S_1$). Thus the equation we use is:

$$I_j = [O_j - 2\ c\ O_jS_1]G$$

where G is a Wiener inverse filter of the form $G = S_o/(S_o^2 + \alpha)$ and α is an empirical constant. The best value for α depends upon the total signal and signal to noise of the images (typical values in the range 0.5–5.0). We use theoretical contrast transfer functions for S_o and S_1 calculated using the equations given by Agard (1984). For calculating S_1 we assume a section spacing (Δz) which serves to control the thickness of the optical sections. The values of the parameters used in generating a particular series of images are given in the figure legends. Typical values used for Δz are 0.5 and 1 μm and for c are 0.48 to 0.50. The criteria used to select the values for Δz and c are discussed in detail in the Discussion. Other parameters for calculating S_o and S_1 are the numerical aperture of the objective lens, the wavelength of emitted light, pixel size, and the index of refraction of the objective immersion oil. The inverse filtering usually introduces some negative values into the images. Therefore, we applied a threshold operation to set negative values to zero (i.e., a nonnegativity constraint).

Modeling of Imaging Properties of the Microscope

Model images were constructed by blurring a series of sections representing the specimen according to the point spread function of the microscope calculated as described above. The models constructed were for 10-μm-diam spherically symmetric cells assuming the three-dimensional model could be represented by a series of sections, 0.1-μm apart. The model for the observed image was calculated using the following equation:

$$O_j = \sum_{k=-60}^{60} I_{j+k}\ S_k$$

where k represents successive sections above (positive k) and below (negative k) the in focus image plane ($k = 0$). An ellipsoidal object with zero intensity was placed in the cell to represent a secretory granule which excludes Ca^{2+} indicator. The deblurring was exactly as described for the real images.

Labeling of Secretory Granules with Quinacrine

Mast cells were labeled with quinacrine by incubating the cells in extracellular medium supplemented with 2.5 μM quinacrine for 5 min. Quinacrine is a convenient fluorescent label for secretory granules because it partitions into acidic compartments. For fluorescence measurements the excitation wavelength was selected with an interference filter centered at 470 nm and the emission a 520-nm long pass filter. The filter block contained a Zeiss 490-nm dichroic mirror.

Measurement of Ca^{2+} Concentration with Fura-2

Mast cells were loaded with the pentapotassium salt of fura-2 using a patch pipette. This is the preferred method because loading with the acetoxymethylester results in a proportion of the indicator entering the secretory granules of mast cells whereas with the pipette the indicator is restricted to the cytosol (Almers and Neher, 1985). The pipette solution contained (in millimolar): 155 K-glutamate, 10 Hepes, 7 $MgCl_2$, 3 KOH, 200 μM ATP, 1 μM GTPγS, and 400 μM fura-2 (290 mmol/kg, pH 7.2). For the optical sectioning experiment (Fig. 5), in which we wanted to prevent Ca^{2+} transients and exocytosis, the ATP and GTPγS were omitted from the loading medium. A fire-polished pipette was used to obtain a giga seal and then gentle suction was used to break into whole cell mode. After 20–30 s, during which the pipette contents were allowed to diffuse into the cell, the patch pipette was pulled away from the cell leaving an intact cell loaded with fura-2 (Almers and Neher, 1985). This period was too short for equilibration of cytosol with the pipette contents, but was long enough to load the cells with sufficient fura-2 with minimal washing out of the cytosolic contents. Fluorescence images of fura-2–loaded cells were collected sequentially at two excitation wavelengths (2-s exposures in Figs. 3 and 6; 5 s in Figs. 4 and 5). The wavelengths were selected with interference filters centered at 350 and 385 nm (10-nm bandwidth at half-maximal transmittance; Omega Optical, Brattleboro, VT), respectively. The filter block of the microscope contained a Zeiss 425 nm dichroic mirror and the emission wavelength was selected with a 480 nm long-pass filter to maximize the amount of light collected. All fura-2 images were acquired on a 128×128 pixel area of the CCD chip corresponding to the position of the cell. Although the cell could have been projected onto a larger area of the CCD chip, this would reduce the amount of light per pixel without increasing the spatial resolution of the image, which is limited by the numerical aperture of the objective. Depending upon the experiment, each pixel corresponded to a square image area of 0.108 or 0.167 μm side.

Ratio fura-2 images are obtained using a three-step procedure: background subtraction, image deblurring, and ratioing. First, a darkfield image is subtracted from both 350- and 385-nm images. The darkfield image was collected with the illumination path shutter closed but with the CCD camera shutter open so that the images are corrected for DC offset, dark current accumulation during the integration and readout time and any stray background light. No correction was made for autofluorescence of the cell, which was negligible, or of the objective which was less than 5% of the total signal. Moreover, the background fluorescence of the optical system is a low frequency component of the image and is effectively removed by the imaging processing procedure. Next the darkfield subtracted 350- and 385-nm images are processed in the Fourier domain using the no neighbors scheme described above. Finally, the ratio of the 350- and 385-nm images is taken in the spatial domain. In most figures the ratio images are shown with no further processing such as thresholding. However, a further improvement in the appearance of the images can be obtained by applying a threshold mask (e.g., the ratio images in Fig. 6), to remove the noisy background ratios that occur in regions where there is no dye. The mask we use is obtained by thresholding the processed 350-nm image at a particular intensity. The 350-nm image is used in preference to the 385-nm image because at this wavelength there is only a small change in the signal during the Ca^{2+} transients. The filtered image is used as it provides a sharp edge to the cells that is relatively insensitive to changing the threshold value, in contrast to the effect of the threshold on the unprocessed image, which undergoes large changes in apparent diameter. The Ca^{2+} calibration used the ratiometric method described by Grynkiewicz et al. (1985):

$$[Ca^{2+}] = K_D\ \beta\ (R - R_{min})/(R_{max} - R)$$

where R is the ratio of fura-2 fluorescence with 350-nm excitation divided by the fluorescence with 385-nm excitation at a given point in time, R_{max} is the ratio when all the fura-2 is bound to Ca^{2+}, R_{min} is the ratio when all the fura-2 is in the free acid form, β is the ratio of fluorescence of free fura-2 divided by the fluorescence of Ca^{2+}-bound fura-2 with 385-nm excitation, and K_D is the dissociation constant for fura-2 and Ca^{2+} binding. The calibration parameters obtained from solutions of fura-2 were as follows: R_{max} = 7.0; R_{min} = 0.19; and β = 23.2. The K_D was assumed to be 224 nM (Grynkiewicz et al., 1985).

Results

The beige mouse is a pigment mutant in which the mast cells have characteristically large secretory granules that can be 3–4 μm across. Apart from being a valuable model system for studying the exocytotic fusion pore (Almers and Breckenridge, 1987; Monck et al., 1990*b*, 1991), the beige mouse mast cell is a useful model for evaluating an imaging system

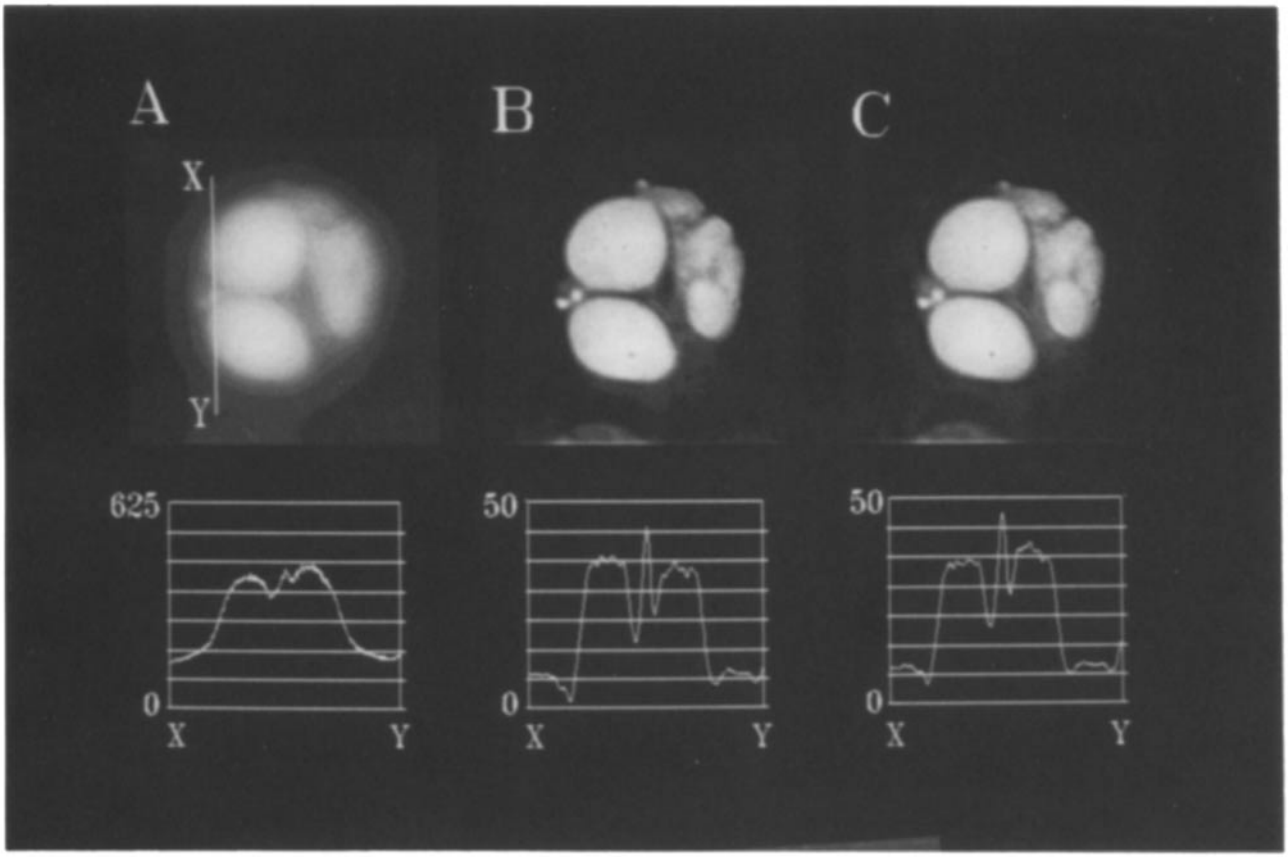

Figure 2. Comparison of the nearest neighbors deblurring scheme with the no-neighbors scheme. (*A*) A high resolution 512 × 512 pixel image of a beige mouse mast cell stained with quinacrine (obtained using a Zeiss Planapo ×63, NA 1.4 objective). Although it can be seen that quinacrine predominantly stains the secretory granules, the edges of the granules are poorly defined due to degradation of the image by the optical system. The profile shows the quinacrine intensity for a line through the two large secretory granules and a small granule as indicated. (*B*) The same cell after processing with the nearest neighbors deblurring scheme. Two neighboring sections taken with a shift in focus 0.5 μm above and below the image plane were used for this procedure. A value of 0.45 was used for c as recommended by Agard (1984). The profile shows that quinacrine intensity is considerably higher in the secretory granules than in the cytosol and that the staining is uniform in the two large granules. (*C*) The same cell after processing with the no neighbors scheme gives an almost identical image to the nearest neighbors scheme. Parameters used for constructing the filters were: c = 0.45, Δz = 0.5 μm; α = 0.5; and pixel size = 0.028 μm.

because the secretory granules and cytosol are distinct structures that can be specifically labeled with fluorescent markers. Fig. 2 *A* shows a conventional epifluorescence image of a beige mouse mast cell stained with quinacrine. Although it is known that quinacrine partitions into the acidic environment inside secretory granules, the structure of the secretory granules cannot be clearly resolved. The intensity profile shows that the granules appear more brightly stained in the center, due to the longer light path in these regions, and that there appears to be significant staining of the cytosol.

Comparison between Nearest Neighbors and No Neighbors Processing Scheme

The nearest neighbor processing scheme uses two adjacent images taken with a known degree of defocus above and below the image plane, to remove out of focus information and extract a deblurred optical section. In a pure optical section, differences in the apparent intensity due to the length of the light path through an object should be abolished. Two different processing schemes were applied to images of the quinacrine stained cell shown in Fig. 2 *A*. The images obtained using the nearest neighbors processing scheme and a modification of this scheme, in which the deblurring requires only a single section, are shown in Figs. 2, *B* and *C*, respectively. The secretory granules can now be seen as distinct structures with in focus edges, in marked contrast to the unprocessed image (Fig. 2 *A*). Moreover, the intensity profiles show that the secretory granules are uniformly stained with quinacrine, indicating that the light path effect has been removed. Thus, both processing schemes can be used to extract thin optical sections from fluorescence images. The only observable difference is that the small secretory granules, for example the cluster of three small granules on the left of the image, appear slightly more blurred in the no neighbors image. The explanation for this difference is that the additional assumption of the no neighbors scheme, that a blurred version of the observed image (O_jS_1) can be used instead of the blurred neighbors ($O_{j+1}S_1$ and $O_{j-1}S_1$), holds better for the larger, lower frequency objects, for which there will be very little difference in the adjacent planes, than for smaller objects, in which the spatial changes occur at a higher frequency. Another common feature of the two processing schemes shown in Fig. 2 is that the smaller objects have a higher intensity than the larger objects. This is because

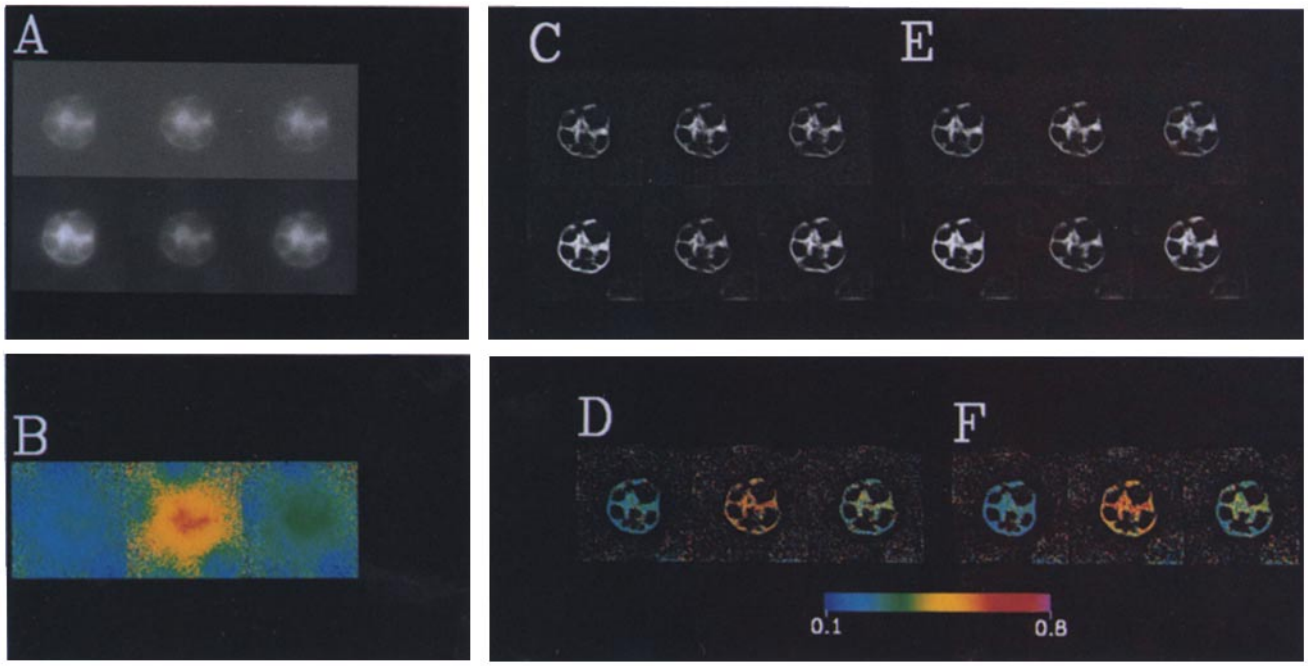

Figure 3.

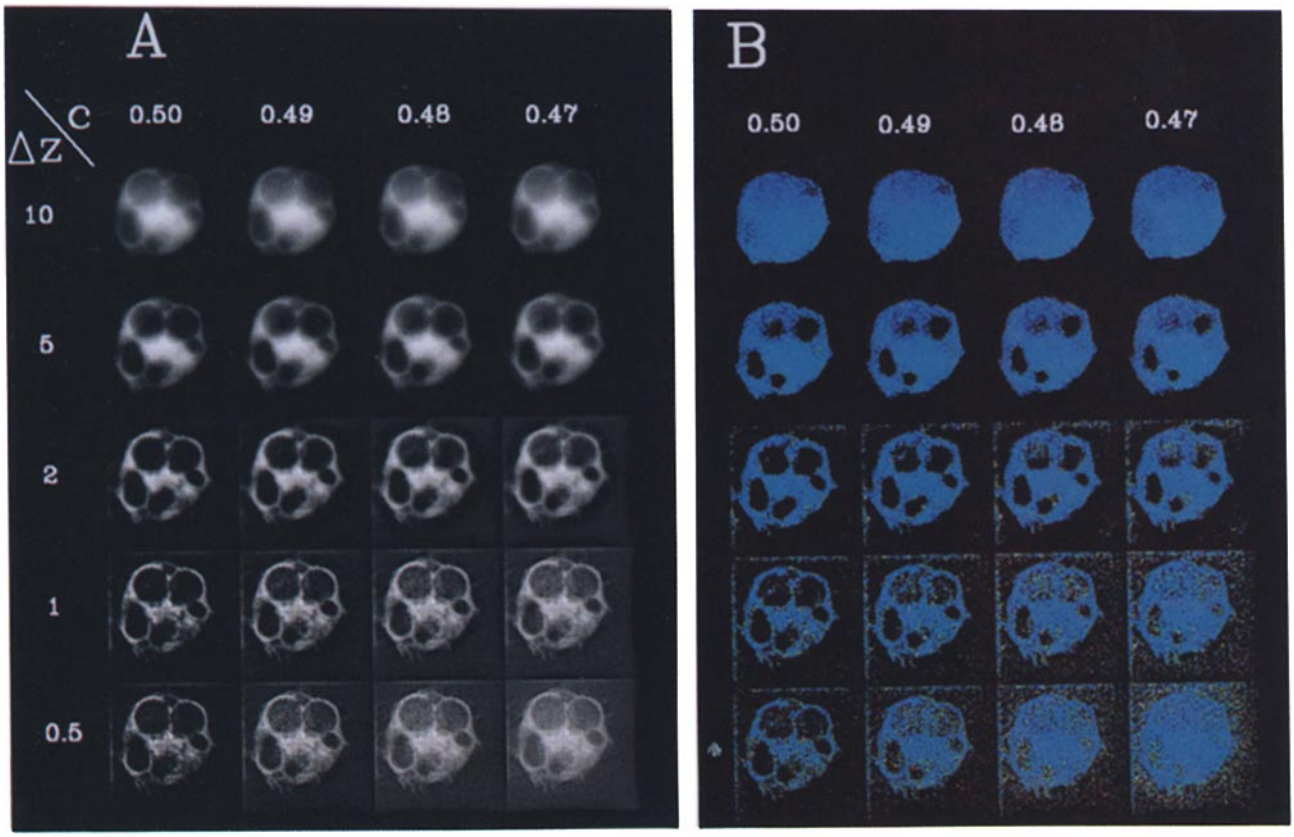

Figure 4.

Figure 3. The effect of processing on the 350 and 385 nm fura-2 images and upon the ratio image. (*A*) The 350 (*top row*) and 385 nm (*bottom row*) images of a fura-2–loaded mast cell before processing. The three images at each wavelength were taken at different times during a Ca^{2+} transient. Although fura-2 is excluded from the secretory granules the edges are not clear. (*B*) The unprocessed ratio images for the three image pairs. The edges of the cell are totally obscure. (*C*) The 350 (*top row*) and 385 nm (*bottom*) images after processing with the Wiener Filter off. The original images are those shown in *A*. The borders between the cytosol and the secretory granules are clearly delineated; it is evident that fura-2 is excluded from the secretory granules. (*D*) The ratio images obtained from the processed 350- and 385-nm images shown in *C*. The edge of the cell is clearly defined and it is possible to see the Ca^{2+} concentration in regions of the cytosol between the secretory granules and the plasma membrane. (*E* and *F*) As *C* and *D* except with the Wiener Filter applied to the images. The color bar is for a linear scale of ratio values between 0.1 and 0.8. Scaling: the display ranges in *A*, *C*, and *E* are different because the inverse filter changes the numbers in the image. However, the relative intensities are retained. The intensities in all the 350-nm images have been doubled to allow comparison with the brighter 385-nm images. The parameters used for constructing the filters were: $c = 0.5$; $\alpha = 5.0$; $\Delta z = 1$ μm, and pixel size = 0.167 μm. No threshold was used on the ratio images. The fura-2–loading solution was supplemented with 200 μM ATP and 1 μM GTPγS. Ratio values of 0.3, 0.5, and 0.8 correspond to Ca^{2+} concentrations of 85, 250, and 510 nM, respectively. Each image panel is a square of 21 μm side.

the out of focus contrast transfer function (S_1) attenuates high frequencies more than low frequencies (see Fig. 6 in Hiraoka et al., 1987). Consequently, when the blurred images are subtracted from the observed image, the effect is equivalent to a high pass filter and proportionately more light is removed from the large objects than the smaller objects. Castleman (1979) has suggested convolving the blurred image with a high pass filter so that the contribution of high and low frequency structures are treated equally. Without such a correction, this property of the processing scheme could be a serious problem for quantitative measurements from a single image. However, for dual excitation wavelength measurements the differential effects on the intensities of different sized objects are similar for both images and consequently are compensated for by the ratio (see Discussion).

Application of the No Neighbors Processing Scheme to Fura-2 Images

Fig. 3 shows the effects of the no neighbors processing scheme on the 350- and 385-nm images of fura-2–loaded mast cells and the ratios derived from these images. As was the case for the quinacrine stained cells (Fig. 2 *A*), the borders between the cytosol and the secretory granules are poorly defined in the unprocessed 350- and 385-nm images (Fig. 3 *A*). The interiors of the secretory granules appear weakly fluorescent as if they contain fura-2. However, we know that there is no fura-2 in the secretory granules because the indicator was loaded with the patch pipette and it is unlikely that the highly negatively charged fura-2 can cross the secretory granules membranes. After processing with the no neighbors scheme, both without (Fig. 3 *C*) and with (Fig. 3 *E*) application of the Wiener Filter, it is clear that fura-2 is excluded from the secretory granules indicating that the out of focus information has been successfully removed.

The ratio images from the unprocessed images show no structure, even though the secretory granules exclude fura-2 and are several microns in diameter (Fig. 3 *B*). In addition, the ratio values extend beyond the boundary of the cell. This is due to residual background light that has not been removed by the background subtraction and to out of focus light originating from fura-2 inside the cell. Since the latter decreases further away from the cell, there is a gradient of ratio values from the cytosol near the cell membrane, which is dominated by the fura-2 fluorescence of the cell, to the edge of the image, which is mainly background fluorescence. This gradient, combined with the lower signal and higher signal to noise near the edge of a cell, explains why there are sometimes artifactual edge effects that give the appearance of a rim of high ratio values. This makes the background subtraction and thresholding, which is usually used to remove signal outside the cell, very important for conventional ratio imaging.

In contrast to the ratio images derived from the unprocessed 350- and 385-nm images, the location of the secretory granules can be clearly seen as regions of the cell where there is no signal when the processed images are used for the ratio image (Figs. 3, *D* and *F*). The processing procedure not only removes the out of focus light originating from the cytosol, but also removes the effect of the background fluorescence. This is because the filters attenuate the low frequency information contained in a uniform background. Thus, when the processed images are used for the ratios, the value of the ratio can be assumed to depend predominantly on the Ca^{2+} concentration of that pixel. Fig. 3 also shows that the Wiener filter does not contribute to the deblurring. Similar deblurring is achieved with the Wiener Filter off (Figs. 3, *C* and *D*) or on (Figs. 3, *E* and *F*). However, the Wiener Filter does, by reducing the noise, significantly improve the quality of the ratio images.

Effect of the Filter Parameters on the Deblurring Efficacy

Fig. 4 shows how varying the values of Δz and c effects the deblurring procedure. A set of 385-nm images (Fig. 4 *A*) and ratio images (Fig. 4 *B*) are shown for Δz values between 10

Figure 4. Effect of filter parameters on the deblurring efficacy of the no neighbors inverse filter. The 385 nm (*A*) and 350/385-nm ratio (*B*) images were obtained for Δz values of 10, 5, 2, 1, and 0.5 μm and for c values of 0.47, 0.48, 0.49, and 0.50. The Wiener Filter used an α value of 0.5 which has only a weak smoothing action so that the effects of the filter parameters on the deblurring can be seen more clearly. An autoscale algorithm was used to display the 385-nm images with maximum contrast. Parameters used for processing: $c = 0.47 - 0.50$; $\Delta z = 0.5 - 10.0$ μm; $\alpha = 0.5$; pixel size = 0.108 μm. Ratio values of 0.3, 0.5 and 0.8 correspond to free Ca^{2+} concentration of 85, 250, and 510 nm.

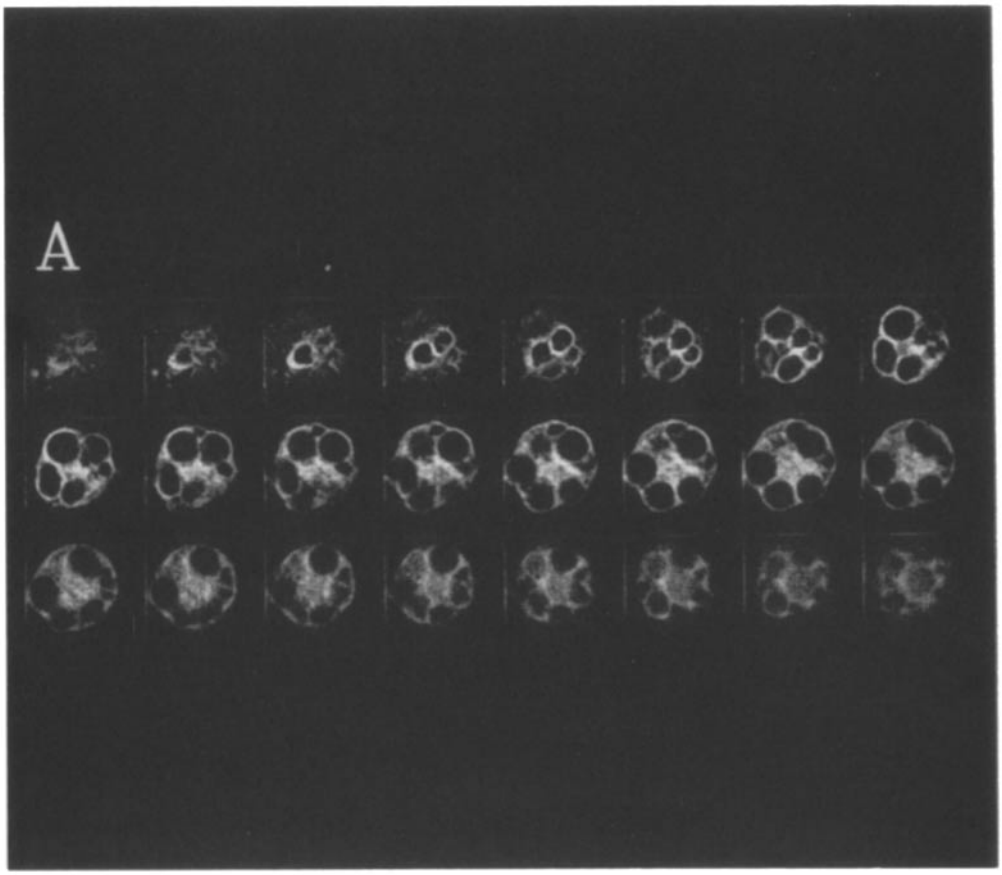

Figure 5. Optical sectioning of a fura-2 loaded beige mouse mast cell. A beige mast cell was loaded with fura-2 using a loading medium without ATP or GTPγS so that Ca^{2+} transients and degranulation would not occur during the sectioning. Pairs of 350- and 385-nm images were taken for a series of sections 0.5-μm apart. (*A*) The 385-nm images starting from near the bottom of the cell (nearest the objective, *top left*) and ending near the top of the cell (*bottom right*). (*B*) The corresponding 350/385-nm ratio images. Parameters used for processing: c = 0.5; Δz = 0.5 μm; α = 0.5; pixel size = 0.108 μm. Ratio values of 0.3, 0.5, and 0.8 correspond to free Ca^{2+} concentrations of 85, 250, and 510 nM, respectively. Each image panel is a 14 × 14 μm square.

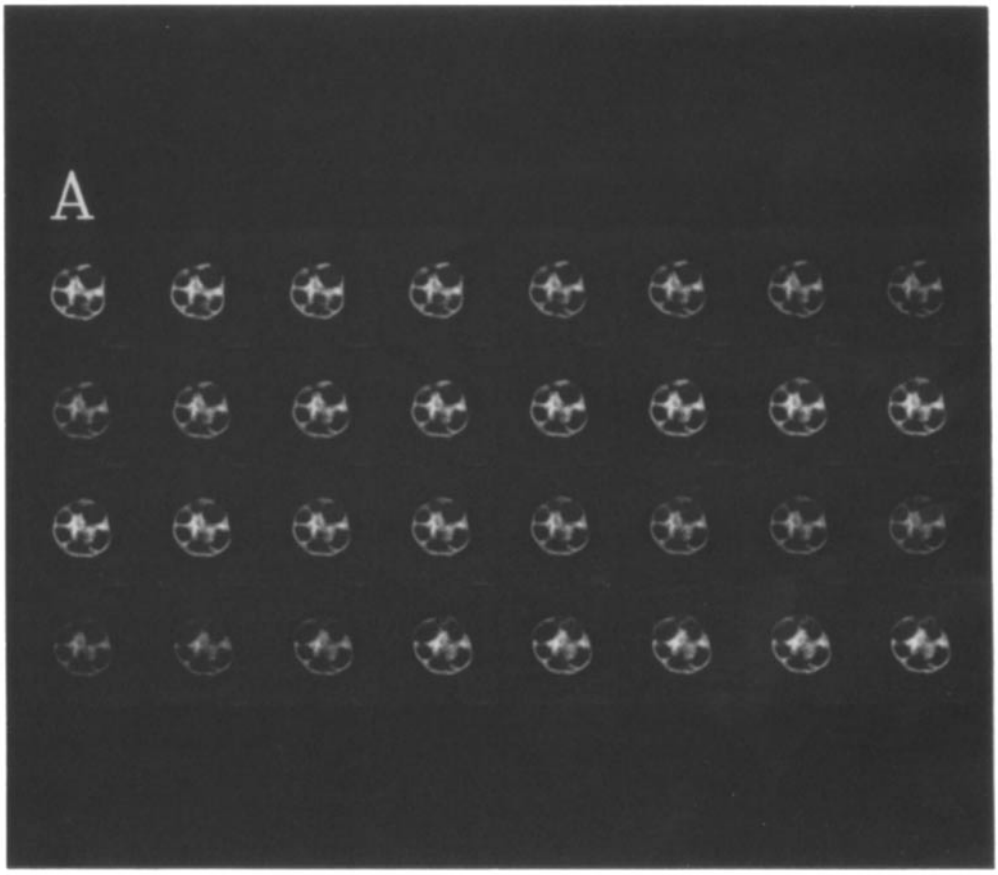

Figure 6. Sequence of 385 nm and ratio images showing Ca^{2+} transients induced by GTPγS. A beige mouse mast cell was loaded with fura in a loading medium containing 200 μM ATP and 1 μM GTPγS to stimulate Ca^{2+} transients and exocytosis. (*A*) A sequence of processed 385-nm images taken 12-s apart. (*B*) The corresponding ratio images. The arrows indicate secretory granules in the frame before they fuse, which can be seen as characteristic swelling of the granule. The parameters used for constructing the filters were as follows: c = 0.49; Δz = 1 μm; α = 5.0; pixel size = 0.167. A threshold mask (made from the 350-nm images) was applied to the ratio images to exclude the speckled background (see Fig. 3 for ratio images from this cell without the mask). Each image panel is a 21 × 21 μm square. The ratio values of 0.3, 0.5, and 0.8 correspond to Ca^{2+} concentrations of 85, 250, and 510 nM, respectively.

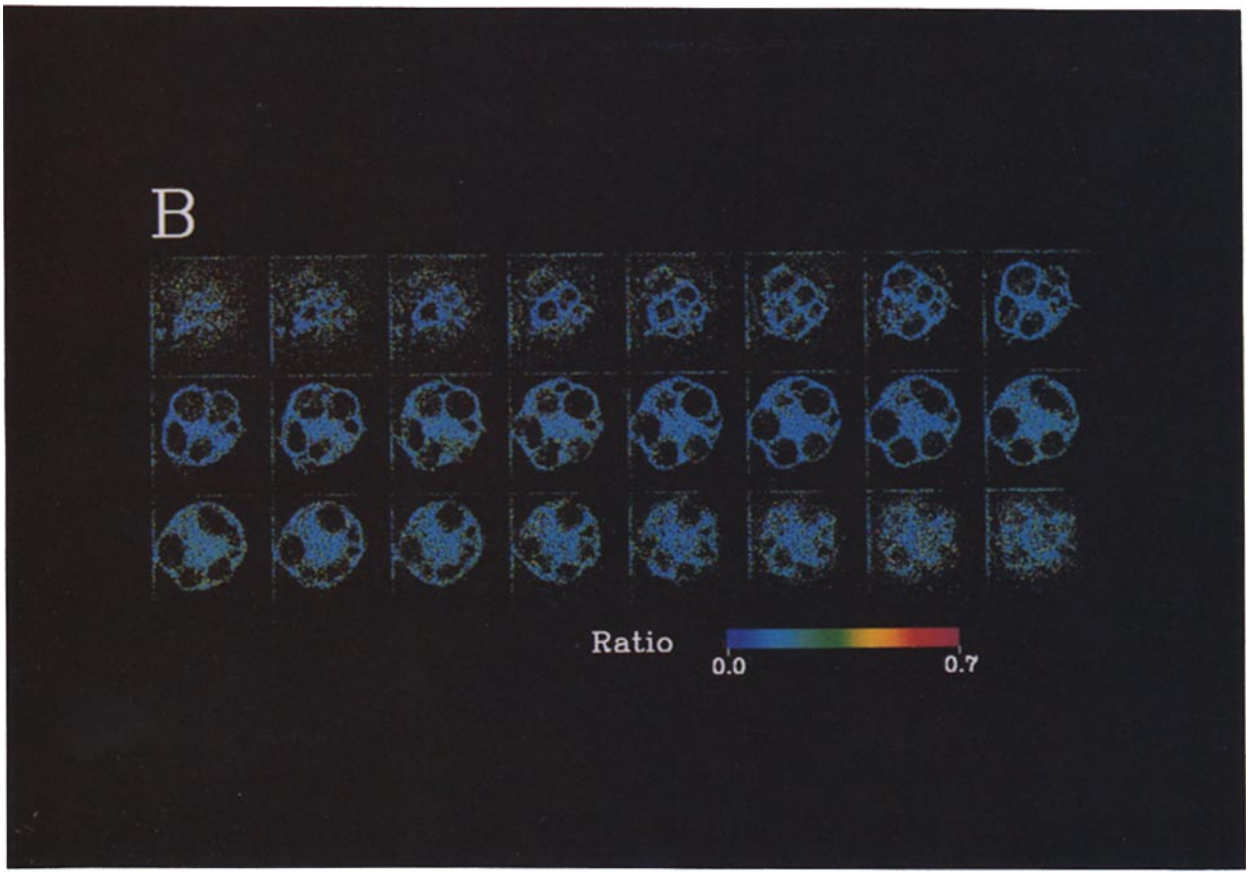

Figure 5.

Figure 6.

and 0.5 μm and for c values between 0.5 and 0.47. Reducing Δz results in a progressive improvement in removal of out of focus information from the secretory granules. With Δz set to 1 μm the best results are obtained since reducing Δz to 0.5 μm increases the noise but has no further improvement on the deblurring. Likewise, increasing c from 0.47 to 0.5 increases the deblurring efficacy. The rationale behind the appropriate choice of filter parameters is discussed in detail in the Discussion section.

Serial Sectioning of a Fura-2 Loaded Mast Cell

Fig. 5 shows an experiment where pairs of 350- and 385-nm images of a fura-2–loaded beige mouse mast cell were taken for a series of sections at different focal planes, each 0.5-μm apart. From the 385-nm images (Fig. 5 *A*) it can be seen that a secretory granule becomes visible in the second section (top line), reaches a maximum size in section 4 and is last seen in section 8. As the granule is visible in seven sections, each 0.5-μm apart, this indicates a diameter of 3 μm in the axial direction. The largest measurable diameter in the image plane is 3 μm (section 5, top line). It is noteworthy that distinct changes in the appearance (apparent size, shape) can be seen in each of the successive images which are separated by only 0.5 μm in the axial direction. A similar analysis of the large granule at the top left of the image, which first appears in section 6, reaches a maximum in section 9, and is no longer visible in section 14, gives a vertical size of ~4 μm, the same as the maximum diameter in the image plane. Again, distinct changes in the appearance of the granule can be seen in each section. The appearance of structures within an image as distinct in focus objects, whose size and shape changes with small shifts in focus, are properties that are expected of a thin optical section.

Time Courses of Ca^{2+} Transients in a GTPγS-stimulated Mast Cell

The mast cell is an extremely important model system because it is possible to simultaneously study the biophysical properties of the fusion pore and the biochemical events involved in stimulating exocytosis. In these cells exocytosis is stimulated by a complex interaction between guanine nucleotides and Ca^{2+}, hence our interest in being able to measure localized changes in Ca^{2+} concentration. A sequence of 385 nm and ratio images for a mast cell stimulated with intracellular GTPγS is shown in Fig. 6. Image pairs were taken 12 s apart. An increase in Ca^{2+} concentration is first evident in section 5, which was taken 380 s after breaking into whole cell mode and allowing GTPγS into the cytosol. It is interesting to note that the GTPγS stimulated Ca^{2+} transient, which is presumably mediated by phospholipase C (Berridge, 1987; Williamson and Monck, 1989), occurs after a significant latent period. This pattern of response is characteristic of sub-maximal agonist-induced Ca^{2+} transients and has been seen in rat basophilic leukemia cells and other cells (Millard et al., 1988; Monck et al., 1988, 1990*a*). The Ca^{2+} concentration increases to a peak level of approximately 400 nM, returns to resting Ca^{2+} levels within ~1 min, and is followed by another transient increase. The magnitude of these increases in the beige mouse mast cell is similar to those previously reported in rat basophilic leukemia cells and rat mast cells; oscillatory patterns of Ca^{2+} concentration were also seen in these cells (Neher and Almers, 1986; Narasimhan et al., 1988; Millard et al., 1989). The ratio images show that the Ca^{2+} increase is relatively uniform across the cell, with similar increases in the center of the cell and in the cytosol between the plasma membrane and secretory granules. It is possible that there is a slightly localized increase in the center of the cell (section 9). However, because the images shown in this figure are for two second exposures at each wavelength, any transient gradients would not have been detected. Nevertheless, the important point demonstrated by Fig. 6 is that it is possible to obtain time courses of ratiometric Ca^{2+} images from thin optical sections, and that it is possible to see a Ca^{2+} increase in a region of cytosol between a secretory granule and the plasma membrane that is <0.5-μm wide.

Morphological Changes Associated with Exocytosis Can Be Observed Simultaneously While Measuring Changes in Ca^{2+} Concentration

Examination of the images shown in Fig. 6 reveals that one of the granules increases in size during the first Ca^{2+} transient; this granule is indicated by the arrow in the section before the granule swells. This increase in granule size is the result of a rapid decondensation of the proteoglycan matrix and histamine contained in the secretory granule when the fusion pore provides a path for entry of Na^+ and water (Monck et al., 1991). A second granule (*arrow*) expands during the second Ca^{2+} transient. Note that one granule (*top right*) had already exocytosed before the experiment started. Thus, our system offers the potential to combine localized measurements of Ca^{2+} concentration and morphological changes associated with the exocytosis of single secretory granules, while at the same time making electrophysiological measurements of membrane conductance changes and capacitance increases that occur as the secretory granules fuse with the plasma membrane.

Discussion

A number of deconvolution algorithms have been developed for correcting images for distortions introduced by the optical system. The best results have been obtained with techniques that utilize a whole stack of two-dimensional images for the deconvolution, such as the full matrix linear filtering approach, constrained iterative methods, and iterative algorithms using nonnegativity constraints based on regularization theory (Castleman, 1979; Agard, 1984; Fay et al., 1989; Agard et al., 1989). However, good results have also been demonstrated for a more simple scheme that only uses adjacent image sections, the nearest neighbors method (Weinstein and Castleman, 1971; Castleman, 1979; Gruenbaum et al., 1984; Agard, 1984). The principal premise of the nearest neighbors scheme is that the contribution of out of focus light can be approximated by assuming that all this light comes from adjacent sections, above and below the in focus plane. These adjacent images are blurred by multiplying their two-dimensional Fourier transforms by the out of focus contrast transfer function (S_1) and then the blurred images are subtracted from the in focus image. Finally, the optical section is obtained by convolving the deblurred image with a Wiener inverse filter. The nearest neighbors algorithm has recently been used to examine Ca^{2+} gradients in fura-2–loaded erythroblasts (Yelamarty et al., 1990).

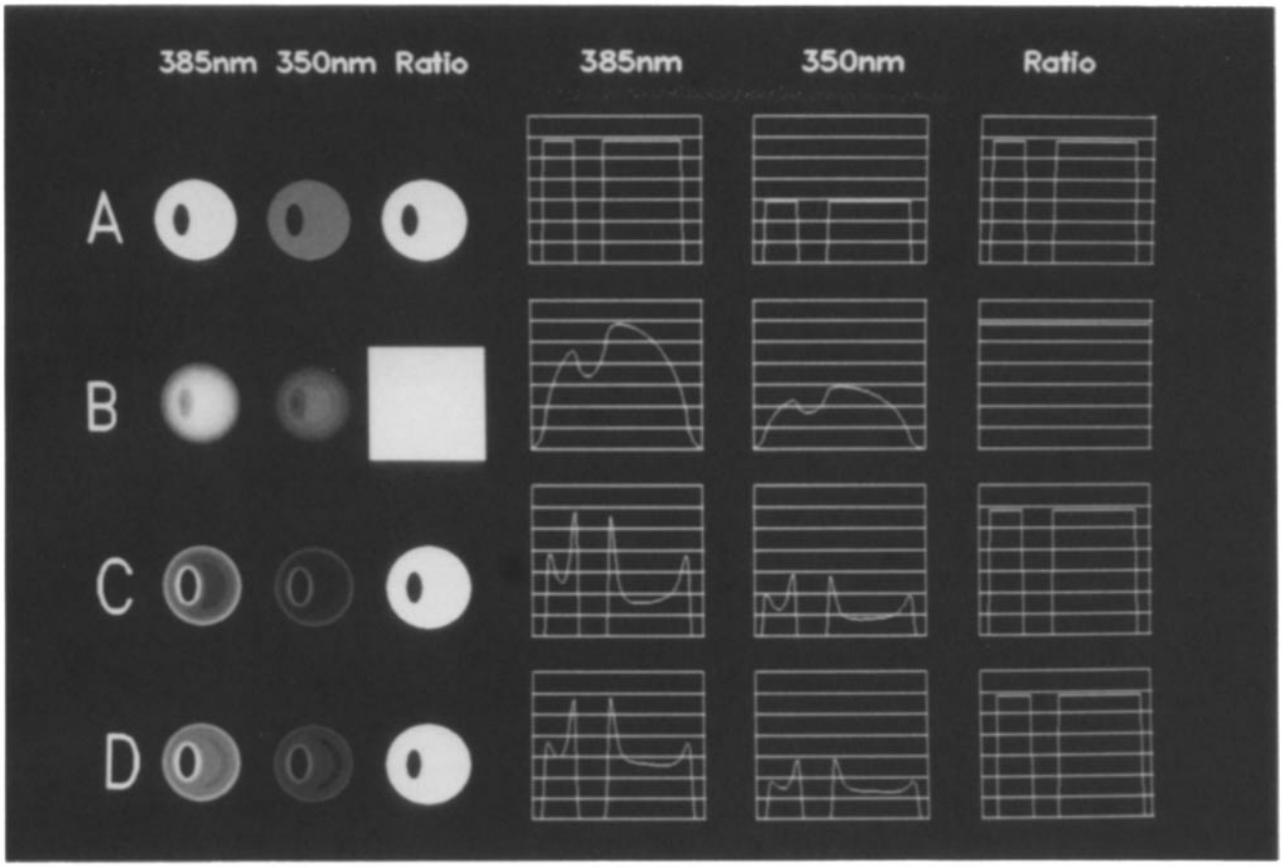

Figure 7. Imaging of a model object with a uniform Ca^{2+} concentration. A model of a cell with a uniform ratio value with a single ellipsoidal granule (radii, 1 and 2 μm in image plane; 2 μm in z direction) with zero intensity was constructed as described in the Methods. (*A, left*) The 385 nm, 350 nm, and ratio images for the model section. (*A, right*) Intensity profiles through the 385 nm, 350 nm, and ratio images. The profiles represent a line through the centers of both the model cell and granule. (*B*) The same sections blurred by convolving with the PSF of the microscope. (*C* and *D*) The blurred sections shown in *B* after application of the no neighbors inverse filter with two different parameter settings. Parameters used for inverse filtering: c = 0.50 (*C*) or 0.49 (*D*); $\Delta z = 1$ μm; $\alpha = 0.5$; and pixel size = 0.108 μm. Each image panel is a 14 × 14 μm square.

Comparison of No Neighbors and Nearest Neighbors Processing Schemes

For real-time fluorescence measurements, it is often not practical to take three or more images to obtain an optical section. Therefore, we tried a modification of the nearest neighbors scheme in which only a single image is used for the deblurring process. Instead of using the neighboring images to obtain the blurred image, we have used the in-focus image itself; that is, we assumed that the blurred version of an image is approximately the same as the blurred version of an adjacent section. The similarity between the processed images of the quinacrine stained mast cell when using the nearest neighbors deblurring scheme (Fig. 2 *B*) and using the no-neighbors scheme (Fig. 2 *C*) demonstrates the validity of this assumption. The main difference between using the in-focus image instead of the neighbors is that the relatively small contributions of high frequency components from neighboring sections are not removed in the deblurring procedure. This effect can be seen in Fig. 2 where the smaller secretory granules (~500-nm diam) appear more blurred in the no neighbors image (Fig. 2 *C*) than in the nearest neighbors image (Fig. 2 *B*). Depending on the application, this small loss of resolution may be of lesser importance when weighed against the improvement in the image contrast and depth of field.

Verification of No Neighbors Inverse Filter with Model Objects

The microscope can be considered as a three-dimensional low-pass filter, which attenuates intensities of high spatial frequency (small objects) more than intensities of low spatial frequency (large objects, out of focus information). The no neighbors processing scheme is a two-dimensional inverse filter for restoring a section through the original object from a single image. The filtering effects of the microscope are illustrated with models in Fig. 7 and 8. The model objects were constructed for a 5-μm radius cell with a single ellipsoid object with zero intensity, to represent a secretory granule with no Ca^{2+} indicator. Fig. 7 *A* shows a section through a model cell with a uniform Ca^{2+} concentration (constant ratio) in the cytosol; the 350- and 385-nm images have uniform intensity as the model corresponds by an infinitely thin section. The blurred images, representing the filtering effect of the microscope, are shown in Fig. 7 *B*. In the single wavelength images, the center of the cell appears brighter than the edge of the cell, and the secretory granule is barely visible. In the ratio image the background and secretory granule have the same ratio as the cytosol, because the light in these parts of the image is out of focus light with the same relative intensities as the cytosol. This explains why the background for the fura-2 ratio image (Fig. 3 *B*) is similar to the value in

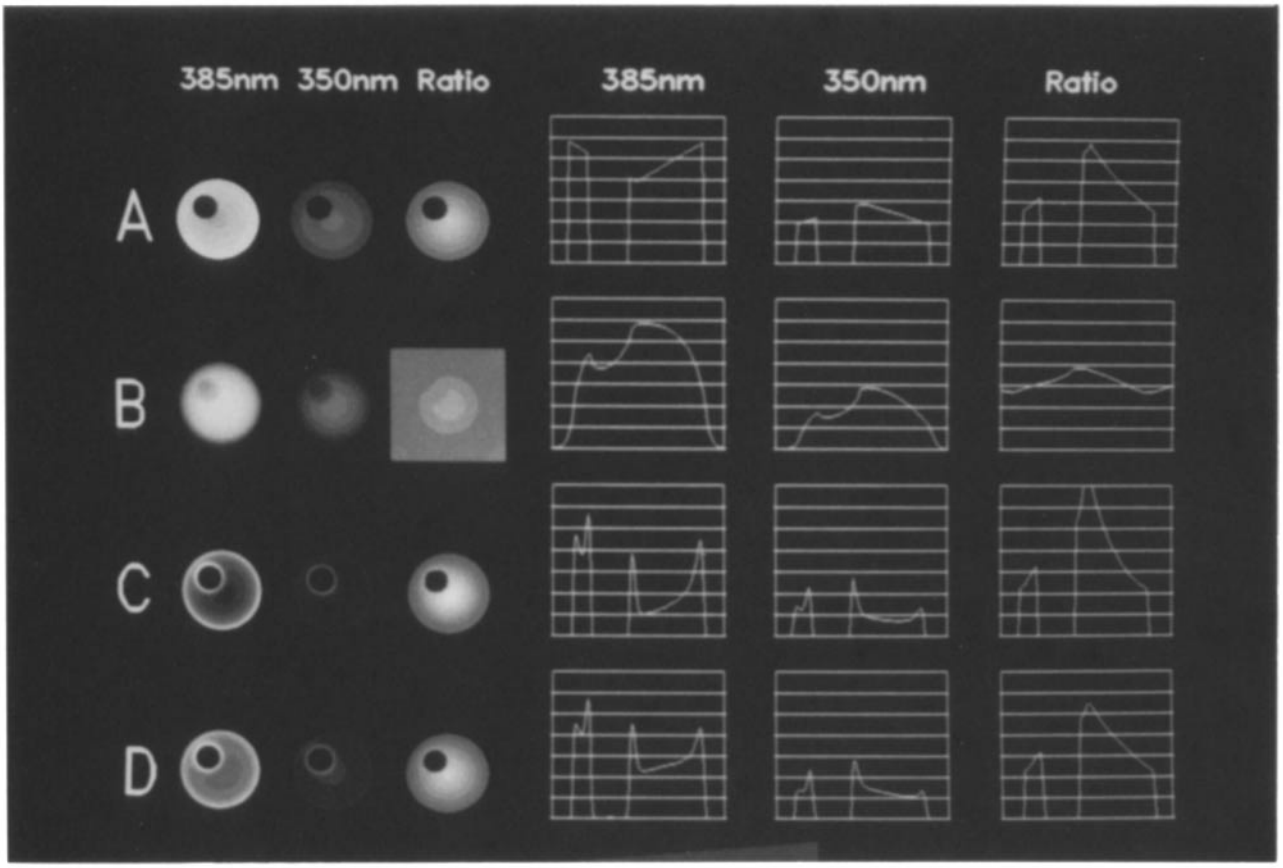

Figure 8. Imaging of a model object with a Ca^{2+} gradient. The gradient was generated by constructing 350- and 385-nm objects with linear gradients as described in Materials and Methods. A spherical (1.5-μm radius) granule with zero intensity was added to the model. (*A*, *left*) The 385 nm, 350 nm, and ratio images for the model section. (*A*, *right*) Intensity profiles through the 385 nm, 350 nm, and ratio images. The profiles represent a line through the centers of both the model cell and granule. (*B*) The same sections blurred by convolving with the PSF of the microscope. (*C* and *D*) The blurred sections shown in *B* after applying the no neighbors inverse filter with two different parameter settings. Parameters used for inverse filtering: c = 0.50 (*C*) or 0.49 (*D*); Δz = 1 μm; α = 0.5; and pixel size = 0.108 μm. Each image panel is a 14 × 14 μm square.

the cell. After applying the no neighbors processing scheme (Figs. 7, *C* and *D*), the location of the secretory granule is clearly defined. However, boundaries of the cytosol, near the secretory granule and plasma membranes, have a higher intensity. This is an edge detector effect of the inverse filter, which also occurs for the nearest neighbors scheme and occurs because an edge comprises high spatial frequencies (see Castleman, 1979). However, in the ratio image (Figs. 7, *C* and *D*) the edge effects have been exactly compensated, because both images have the same spatial frequencies. Thus, in this example, ratio imaging exactly compensates for the distortions introduced by the inverse filtering scheme.

Another model, in which there is a gradient of Ca^{2+} from a high value at the center of the cell to a low value at the edge of the cell, is shown in Fig. 8. The model was constructed from two fluorescence images with linear gradients of intensity (Fig. 8 *A*). The blurred model (Fig. 8 *B*), again shows that the secretory granule is poorly defined. However, more importantly, the ratio values in the blurred model are different from those in the model object. The ratio at the edge of the cell is approximately correct, but the ratio at the center of the cell is too small. This model clearly demonstrates how the magnitude of a Ca^{2+} gradient is distorted by the filter function of the microscope.

Two image reconstructions using slightly different filters are shown in Fig. 8, *C* and *D*, respectively. In Fig. 8 *C* the value of c was set at 0.5 to remove all the background signal (spatial frequencies near zero). In the ratio image the edge of the cell has the correct value, but the ratio at the center is now over estimated (compare with Fig. 8 *A*). The images in Fig. 8 *D* were obtained using a filter with c set at 0.49. The edge effects are still apparent in the single wavelength images, but the ratio image is a good estimate of the ratio image obtained from the original sections. We have constructed a number of different models representing mast cells with different gradients and with ellipsoid granules of different size and aspect, centered both in and out of the plane of focus. In all models a value of 0.49 always gave a significantly better estimate of the original ratio than the ratio image obtained after blurring the model object by the transfer function of the microscope which represents the unprocessed ratio.

Application of No Neighbors Scheme to Fura-2 Images

In the unprocessed 350- and 385-nm images of fura-2–loaded mast cells, the secretory granules can be seen as regions of lower intensity fluorescence, although the edges of the granules are not resolved (Fig. 3 *A*). It is not obvious

whether the granules exclude the indicator or contain fura-2 at lower concentrations than the cytosol, although it is expected that the negative charges on the fura-2 molecules should prevent them crossing the secretory granule membrane. On the other hand, when the images have been processed the edges of the granules become clearly defined and it is now clear that the secretory granules exclude the indicator (Fig. 3 *C*). When the unprocessed images are used for the ratio, no structure can be seen in the ratio image (Fig. 3 *B*). The secretory granules appear to have a similar ratio to the surrounding cytosol because the ratio is largely determined by the out of focus light originating from points in the cytosol (compared with the model objects; Figs. 7 *B* and 8 *B*). When the processed images are used for the ratio the structure of the cell becomes clearly resolved. Not only are the secretory granules and cell edges clearly defined, but the ratio outside the boundary of the cell due to the background fluorescence, which is the lowest frequency component of the image, has been removed by the inverse filtering procedure.

When applying an inverse filtering scheme to real images, the selection of the appropriate filter parameters is critical. The no neighbors processing scheme uses three variable parameters: Δz, the amount of defocus used to calculate the out-of-focus PSF (S_1) used in the deblurring algorithm; c, the constant determining the amount of deblurring; and α, which is used in the Wiener filter. However, as shown in Fig. 3 (compare *B* and *C*), the Wiener filter improves the signal to noise of the final image, but has no significant effect on the deblurring. Therefore, the value selected for α is not critical. Fig. 4, which shows the effect of different filters using Δz between 10 and 0.5 μm and c between 0.47 and 0.5, illustrates how appropriate values of Δz and c can be selected. When Δz is set at 10 μm there is little deblurring, although with c = 0.5 the background is removed because it has the lowest spatial frequencies. Reducing Δz from 10 to 1 μm results in progressive improvements in removal of out of focus information from the secretory granule (see the column for c set at 0.5). Further reducing Δz from 1 to 0.5 μm yields no further improvement, but decreases the signal to noise. Therefore, the optimum choice for Δz for these images is 1 μm. With this approach there is little danger of generating artifacts with the inverse filter because the filter is being used to increase the contrast of objects that are already visible, albeit poorly, in the original image. Increasing c from 0.47 to 0.50 also progressively improves the removal of out of focus haze. The models (Figs. 7 and 8) suggest that c = 0.49 gives the best quantitative results for a 10 μm diameter cell and, for this reason, we used c = 0.49 in Fig. 6.

The Processed Images Have the Properties of a Thin Section

In a thin optical section the intensity of a fluorescently labeled structure should not be affected by the path length through that structure, as is the case for conventional epifluorescence images with their large depth of field (see models in figs. 7 *B* and 8 *B*), and all structures within the image should appear as in focus objects, regardless of their position in the image plane. The first characteristic is demonstrated in Fig. 2 which shows that, after processing with either the nearest neighbors or no neighbors deblurring schemes, the quinacrine stained secretory granules are uniformly labeled, whereas before processing the fluorescence intensity is clearly brighter in the centers, where the path length through the granule is longer. Fig. 5 shows that distinct changes in the size and shape of the excluded areas representing the secretory granules can be seen in adjacent sections taken at 0.5-μm separation. It is noteworthy that the edges of the granules appear in focus, except at the top and bottom of the granules where edges become blurred because of the greater curvature. These properties together demonstrate a depth of field of $\sim$1 μm, which is a marked improvement over the depth of field in the unprocessed epifluorescence image. The larger depth of field of the fluorescence measurements usually results in an object appearing elongated in the axial direction when a series of sections at different focal planes are taken through an object. However, in the images obtained using the no neighbors deblurring scheme (Fig. 5), the maximum diameters measurable in the axial direction are similar to the maximum diameter in the image plane.

Advantages and Disadvantages of the No Neighbors Scheme for Ca^{2+} Measurements

The recent excitement in the development of the scanning confocal microscope is because of the ability of this instrument, using a confocal optical system, to generate thin optical sections. Because the images generated by the no neighbors processing scheme share some of the properties of the images collected using the scanning confocal microscope, it is interesting to consider the relative advantages and disadvantages of our computational procedure compared to the use of various types of scanning confocal microscope for different experimental situations. When light intensity is not a problem there can be no doubt that the scanning confocal microscopes are unsurpassed for producing high contrast images at high spatial resolution (White et al., 1987; Brakenhoff et al., 1989; Wright et al., 1989). However, for low light applications where temporal resolution is also important, such as in measurements of Ca^{2+} concentration, a number of compromises must be made and the choice becomes less clear (Wright et al., 1989; Carrington et al., 1990).

The first consideration is the intensity of the signal and temporal resolution. The fura-2 images shown in this paper were all 128 × 128 pixel images and, for the time course shown in Fig. 6, light was collected from each pixel for an exposure time of 2 s. The mean intensity values read out from the CCD chip were 70 and 300 for the 350 and 385 nm, respectively, in resting cells. For our camera this corresponds to about 2,200 and 9,500 photons/pixel for the two images. We estimate that to obtain 2,200 photons at the detector there must be of the order of 1–3 × 10^4 photons emitted from the fura-2 in the cell. In our experiments, the major limitation governing the intensity of the images is the fraction of light entering the light guide coupling the mercury arc lamp to the microscope, which is only $\sim$4%. By focusing the image of the arc lamp (area = 0.25 × 0.25 mm) onto the end of the light guide, it should be possible to obtain equivalent quality images to those shown in about 100 ms. The limit of temporal resolution should be obtained when the illumination intensity is high enough to excite the fluorophores so rapidly that few molecules are left in the ground state. This could be achieved using a laser illumination sys-

tem. Hibino et al. (1991), have obtained sub-microsecond images of transmembrane potential using a pulsed laser, which is defocused to illuminate the whole field of view for the 300-ns duration of the pulse. A pulsed laser can readily supply the energy needed to saturate the fluorophore (Hibino et al., 1991; Keating and Wensel, 1991). For 400 μM fura-2 in a volume of 2.8×10^{-16} liters (pixel area $\times$ depth of field) there will be about 7×10^4 excited fura-2 molecules, which would yield 2×10^4 photons for each activation, assuming a quantum efficiency of 0.31 for fura-2 at 100 nM-free Ca^{2+} (Grynkiewicz et al., 1985). Since the fluorescence lifetime of fura-2 is $\sim$2 ns (Keating and Wensel, 1991) each fura-2 molecule could contribute up to 25 photons during a 50-ns pulse. This would provide sufficient photons to generate images of considerably higher quality than those shown in Figs. 3–6. Thus, the combination of our inverse filtering approach with pulsed laser imaging techniques (Hibino et al., 1991; Keating and Wensel, 1991) offers the potential to obtain thin section images in less than a microsecond. This contrasts with the scanning confocal microscopes where the requirement to scan the image necessitates excitation intensities at least three or four orders of magnitude higher than with the conventional epifluorescence microscope or, where fluorescence saturation is limiting, an equivalent reduction in temporal resolution.

Another consideration for measurements of intracellular Ca^{2+} concentration is the choice of Ca^{2+} indicator. One of the most important factors that has recently made measurements in single cells feasible has been the availability of the ratiometric indicators, fura-2 and indo-1 (Grynkiewicz et al., 1985; Tsien, 1989). Fura-2, the most widely used indicator for Ca^{2+} imaging, is unsuitable for confocal microscopy because it requires two excitation wavelengths. Indo-1 requires two emission wavelengths and is suitable, but at the time of writing, no studies using indo-1 with a scanning confocal microscope have been published. This might be a result of technical problems of using an ultraviolet laser with commercially available scanning confocal microscopes, to problems of aligning two separate exit pinholes so that the two detectors see both wavelengths at the same focal plane, to dye saturation, or due to photobleaching or photocytotoxicity problems (Wells et al., 1990; Tsien and Waggoner, 1990). An alternative is to use fluo-3, an indicator that is excited by visible wavelengths of light (Minta et al., 1989). However, unlike with fura-2 and indo-1, the binding of Ca^{2+} to fluo-3 does not induce any useful shifts in the excitation and emission spectra that can be used for ratiometric calibration of the intracellular Ca^{2+} concentration. Fluo-3 has been used with a laser scanning confocal microscope to measure the Ca^{2+} concentration in sympathetic neurons and cardiac myocytes (Hernandez-Cruz et al., 1990; Niggli and Lederer, 1990), and with a tandem scanning confocal microscope in mouse oocytes (Wright et al., 1989). The large size of these cell types probably enabled detection of an adequate signal. It remains to be seen if such studies are possible with smaller cells at high spatial resolution.

Conclusion

By using a computational method to remove out of focus information from fluorescence images of fura-2–loaded mast cells, we have been able to obtain time resolved high resolution ratiometric Ca^{2+} images corresponding to thin optical sections through the cell. The no neighbors deblurring scheme has been verified by: (*a*) comparing the technique with an established method, the nearest neighbors algorithm; (*b*) showing a serial sectioning experiment in which the properties of a thin optical section are demonstrated; (*c*) generating model objects, simulating the blurring due to the transfer function of the microscope and applying the no neighbors inverse filter to restore the original object; (*d*) showing the effect of varying the filter parameters on experimental and model data; and (*e*) showing how the combination of ratio imaging with the no neighbors processing removes some of the inherent limitations of the inverse filtering. An important advantage of this approach is that it does not require a sequence of serial sections, which requires special equipment and greatly reduces the time resolution, and is applicable to any image obtained by a conventional epifluorescence microscope. The technique can be also applied retrospectively to images that have already been collected. The only additional pieces of equipment required, apart from the microscope itself, are a 12-bit CCD camera and a microcomputer system capable of performing two-dimensional Fourier transforms. Such a system has the additional advantage that it can readily be adapted for use of different indicators using different excitation and emission wavelengths and should be suitable for multi-parameter studies using several different indicators simultaneously (DeBiasio et al., 1989).

We would like to thank Drs. David Agard, Fred Fay, and Roger Tsien for critical reading of the manuscript and helpful suggestions. We would also like to thank Jay Copeland for assistance with the modelling and Mahlon Stacy for advice on the use of ANALYZE. We are indebted to Cindy Camrud for secretarial assistance and Marilyn Waldschmidt for technical assistance.

This work was supported by the National Institute of Health Grant GM-38857 and by the Mayo Foundation. We thank the Whitaker Foundation for a grant for development of the microscope system. J. M. Fernandez is an Established Investigator of the American Heart Association.

Received for publication 10 January 1991 and in revised form 15 August 1991.

References

Agard, D. 1984. Optical sectioning microscopy: cellular architecture in three dimensions. *Annu. Rev. Biophys. Bioeng.* 13:191–219.

Agard, D. A., Y. Hiraoka, P. Shaw, and J. W. Sedat. 1989. Fluorescence microscopy in three dimensions. *Meth. Cell Biol.* 30:353–377.

Almers, W., and E. Neher. 1985. The Ca signal from fura-2 loaded mast cells depends strongly on the method of dye-loading. *FEBS (Fed. Eur. Biol. Soc.) Lett.* 192:13–18.

Berridge, M. J. 1987. Inositol trisphosphate and diacylglycerol: two interacting second messengers. *Annu. Rev. Biochem.* 56:159–193.

Brakenhoff, G. J., E. A. Van Spronsen, H. T. M. Van Der Voort, and N. Nanninga. 1989. Three-dimensional confocal fluorescence microscopy. *In* Methods in Cell Biology. Academic Press, Inc., Orlando, FL. 379–398.

Breckenridge, L. J., and W. Almers. 1987. Currents through the fusion pore that forms during exocytosis of a secretory vesicle. *Nature (Lond.).* 328: 814–817.

Carrington, W. A., K. E. Fogarty, L. Lifschitz, and F. S. Fay. 1990. Three-dimensional imaging on confocal and wide-field microscopes. *In* Handbook of Biological Confocal Microscopy. J. B. Pawley, editor. Plenum Publishing Corp., New York. 151–161.

Castleman, K. R. 1979. Digital Image Processing. Prentice-Hall, Inc., Englewood Cliffs, NJ. 429 pp.

Cohan, C. S., J. A. Connor, and S. B. Kater. 1987. Electrically and chemically mediated increases in intracellular calcium in neuronal growth cones. *J. Neurosci.* 7:3588–3599.

Connor, J. A., M. C. Cornwall, and G. H. Williams. 1987. Spatially resolved cytosolic calcium response to angiotensin II and potassium in rat glomerulosa cells measured by digital imaging techniques. *J. Biol. Chem.* 262:2919–2927.

Cornell-Bell, A. H., S. M. Finkbeiner, M. S. Cooper, and S. J. Smith. 1990. Glutamate induces calcium waves in cultured astrocytes: long-range glial signaling. *Science (Wash. DC).* 247:470–473.

DeBiasio, R., G. R. Bright, L. A. Ernst, A. S. Waggoner, and D. Lansing Taylor. 1987. Five-parameter fluorescence imaging: wound healing of living Swiss 3T3 cells. *J. Cell Biol.* 105:1613–1622.

Fay, F. S., W. Carrington, and K. E. Fogarty. 1989. Three-dimensional molecular distribution in single cells analyzed using the digital imaging microscope. *J. Microscopy.* 153:133–149.

Gruenbaum, Y., M. Hochstrasser, D. Mathog, H. Saumweber, D. A. Agard, and J. W. Sedat. 1984. Spatial organization of the *Drosophila* nucleus: a three-dimensional cytogenetic study. *J. Cell Sci. Suppl.* 1:223–234.

Grynkiewicz, G., M. Poenie, and R. Y. Tsien. 1985. A new generation of Ca^{2+} indicators with greatly improved fluorescent properties. *J. Biol. Chem.* 260:3440–3450.

Hernandez-Cruz, A., F. Sala, and P. R. Adams. 1990. Subcellular calcium transients visualized by confocal microscopy in a voltage-clamped vertebrate neuron. *Science (Wash. DC).* 247:858–862.

Hibino, M., M. Sigemori, H. Itoh, K. Nagayama, and K. Kinosita, Jr. 1991. Membrane conductance of an electroporated cell analyzed by submicrosecond imaging of transmembrane potential. *Biophys. J.* 59:209–220.

Hiraoka, Y., J. W. Sedat, and D. A. Agard. 1987. The use of a charge-coupled device for quantitative optical microscopy of biological structures. *Science (Wash. DC).* 238:36–41.

Inoue, S. 1990. Foundations of confocal imaging in light microscopy. *In* Handbook of Biological Confocal Microscopy. J. B. Pawley, editor. Plenum Publishing Corp., New York. 1–14.

Keating, S. M., and T. G. Wensel. 1991. Nanosecond fluorescence microscopy. Emission kinetics of Fura-2 in single cells. *Biophys. J.* 59:186–202.

Lichtman, W., S. J. Sunderland, and R. S. Wilkinson. 1989. High-resolution imaging of synaptic structure with a simple confocal microscope. *The New Biol.* 1:75–82.

Lipscombe, D., D. V. Madison, M. Poenie, H. Reuter, R. Y. Tsien, and R. W. Tsien. 1988. Spatial distribution of calcium channels and cytosolic calcium transients in growth cones and cell bodies of sympathetic neurons. *Proc. Natl. Acad. Sci. USA.* 85:2398–2402.

Millard, P. J., D. Gross, W. W. Webb, and C. Fewtrell. 1988. Imaging asynchronous changes in intracellular Ca^{2+} in individual stimulated tumor mast cells. *Proc. Natl. Acad. Sci. USA.* 85:1854–1858.

Millard, P. J., T. A. Ryan, W. W. Webb, and C. Fewtrell. 1989. Immunoglobulin E receptor cross-linking induces oscillations in intracellular free ionized calcium in individual tumor mast cells. *J. Biol. Chem.* 264:19730–19739.

Minta, A., J. P. Y. Kao, and R. Y. Tsien. 1989. Fluorescent indicators for cytosolic calcium based on rhodamine and fluorescein chromophores. *J. Biol. Chem.* 264:8171–8178.

Monck, J. R., E. E. Reynolds, A. P. Thomas, and J. R. Williamson. 1988. Novel kinetics of single cell Ca^{2+} transients in stimulated hepatocytes and A10 cells measured using fura-2 and fluorescent videomicroscopy. *J. Biol. Chem.* 263:4569–4575.

Monck, J. R., R. E. Williamson, I. Rogulja, S. J. Fluharty, and J. R. Williamson. 1990*a*. Angiotensin II effects on the cytosolic free Ca^{2+} concentration in N1E-115 neuroblastoma cells: kinetic properties of the Ca^{2+} transient measured in single fura-2 loaded cells. *J. Neurochem.* 54:278–287.

Monck, J. R., G. Alvarez de Toledo, and J. M. Fernandez. 1990*b*. Tension in secretory granule membranes causes extensive membrane transfer through the exocytotic fusion pore. *Proc. Natl. Acad. Sci. USA.* 87:7804–7808.

Monck, J. R., A. Oberhauser, G. Alvarez de Toledo, and J. M. Fernandez. 1991. Is swelling of the secretory granule matrix the force that dilates the exocytotic fusion pore? *Biophys. J.* 59:39–47.

Narasimhan, V., D. Holowka, C. Fewtrell, and B. Baird. 1988. Cholera toxin increases the rate of antigen-stimulated calcium influx in rat basophilic leukemia cells. *J. Biol. Chem.* 263:19626–19632.

Neher, E., and W. Almers. 1986. Fast calcium transients in rat peritoneal mast cells are not sufficient to trigger exocytosis. *EMBO (Eur. Mol. Biol. Organ.) J.* 5:51–53.

Niggli, E., and W. J. Lederer. 1990. Real-time confocal microscopy and calcium measurements in heart muscle cells: towards the development of a fluorescence microscope with high temporal and spatial resolution. *Cell Calcium.* 11:121–130.

O'Sullivan, A. J., T. R. Cheek, R. B. Moreton, M. J. Berridge, and R. D. Burgoyne. 1989. Localization and heterogeneity of agonist-induced changes in cytosolic calcium concentration in single bovine adrenal chromaffin cells from video imaging of fura-2. *EMBO (Eur. Mol. Biol. Organ.) J.* 8:401–411.

Rooney, T. A., E. J. Sass, and A. P. Thomas. 1990. Agonist-induced cytosolic calcium oscillations originate from a specific locus in single hepatocytes. *J. Biol. Chem.* 265:10792–10796.

Shotton, D. M. 1989. Confocal scanning optical microscopy and its application for biological specimens. *J. Cell Sci.* 94:175–206.

Tsien, R. Y., and A. Waggoner. 1990. Fluorophores for confocal microscopy: photophysics and photochemistry. *In* Handbook of Biological Confocal Microscopy, J. B. Pawley, Editor, Plenum Publishing Corp., New York. 169–178.

Tsien, R. Y. 1980. New calcium indicators and buffers with high selectivity against magnesium and protons: design, synthesis, and properties of prototype structures. *J. Biochem.* 19:2396–2404.

Tsien, R. Y. 1989. Fluorescent indicators of ion concentrations. *In* Methods in Cell Biology: Fluorescent Microscopy of Living Cells in Culture. D. Lansing Taylor and Y. L. Wang, editors. Academic Press Inc., Orlando, FL. 127–156.

Weinstein, M., and K. R. Castleman. 1971. Reconstructing 3-D specimens from 2-D section images. *Proc. Soc. Photo-Opt Instr. Engng.* 26:131–138.

Wells, K. S., D. R. Sandison, J. Strickler, and W. W. Webb. 1990. Quantitative fluorescence imaging with laser scanning confocal microscopy. *In* Handbook of Biological Confocal Microscopy. J. B. Pawley, Editor. Plenum Publishing Corp., New York. 27–39.

White, G. B., W. B. Amos, and M. Fordham. 1987. An evaluation of confocal versus conventional imaging of biological structures by fluorescence light microscopy. *J. Cell Biol.* 105:41–48.

Wier, W. G., M. B. Cannell, J. R. Berlin, E. Marban, and W. J. Lederer. 1987. Cellular and subcellular heterogeneity of $[Ca^{2+}]_i$ in single heart cells revealed by fura-2. *Science (Wash. DC).* 235:325–328.

Williams, D. A., K. E. Fogarty, R. Y. Tsien, and F. S. Fay. 1985. Calcium gradients in single smooth muscle cells revealed by the digital imaging microscope using fura-2. *Nature (Lond.).* 318:558–561.

Williamson, J. R., and J. R. Monck. 1989. Hormone effects on cellular Ca^{2+} fluxes. *Annu. Rev. Physiol.* 51:107–124.

Wright, S. J., J. S. Walker, H. Schatten, C. Simerly, J. J. McCarthy, and G. Schatten. 1989. Confocal fluorescence microscopy with the tandem scanning light microscope. *J. Cell Sci.* 94:617–624.

Yelamarty, R. V., B. A. Miller, R. C. Scaduto, Jr., F. T. S. Yu, D. L. Tillotson, and J. Y. Cheung. 1990. Three-dimensional intracellular calcium gradients in single human burst-forming units-erythroid-derived erythroblasts induced by erythropoietin. *J. Clin. Invest.* 85:1799–1808.